

ACCRETION OF SOLID MATERIALS ONTO CIRCUMPLANETARY DISKS FROM PROTOPLANETARY DISKS

TAKAYUKI TANIGAWA

Institute of Low Temperature Science, Hokkaido University, Sapporo, 060-0819, Japan

AND

AKITO MARUTA AND MASAHIRO N. MACHIDA

Department of Earth and Planetary Sciences, Kyushu University, Fukuoka 812-8581, Japan

Draft version January 20, 2014

ABSTRACT

We investigate accretion of solid materials onto circumplanetary disks from heliocentric orbits rotating in protoplanetary disks, which is a key process for the formation of regular satellite systems. In the late stage of gas-capturing phase of giant planet formation, the accreting gas from protoplanetary disks forms circumplanetary disks. Since the accretion flow toward the circumplanetary disks affects the particle motion through gas drag force, we use hydrodynamic simulation data for the gas drag term to calculate the motion of solid materials. We consider wide range of size for the solid particles (10^{-2} - 10^6 m), and find that the accretion efficiency of the solid particles peaks around 10m-sized particles because energy dissipation of drag with circum-planetary disk gas in this size regime is most effective. The efficiency for particles larger than 10m size becomes lower because gas drag becomes less effective. For particles smaller than 10m, the efficiency is lower because the particles are strongly coupled with the back-ground gas flow, which prevent particles from accretion. We also find that the distance from the planet where the particles are captured by the circumplanetary disks is in a narrow range and well described as a function of the particle size.

Keywords: planets and satellites: formation — protoplanetary disks

1. INTRODUCTION

The giant planets in our solar system have many natural satellites. In terms of mass, most of the satellites are categorized into regular satellites, which are rotating in almost circular and co-planer with the equatorial planes of the parent planets. Because of the regularity, the satellites are believed to be formed in circumplanetary disks, which would have existed when the giant planet were forming in the protoplanetary disk.

Thus the satellite systems had been considered to have formed in an isolated and closed disk that have enough mass to produce the current systems (Lunine & Stevenson 1982). This is so-called Minimum Mass Sub Nebula (MMSN) disk model. However, the formation through such a heavy disk leads to some difficulties in its formation processes, such as too high temperature for H₂O to be solid phase, too fast type I migration for satellites, and too short accretion timescale for Callisto's internal structure not to be fully differentiated (Canup & Ward 2002).

In order to overcome these problems, two further models to describe circumplanetary disks are proposed. One is a gas-starved disk model (Canup & Ward 2002, 2006; Ward & Canup 2010), which is an open disk model. This means that the disk receives continuous mass supply from the protoplanetary disk, and is much less massive than the MMSN-type disk. This model solves several serious problems that could not solve by MMSN-type disk model (Canup & Ward 2002). Another is solids-enhanced minimum mass (SEMM) model (Mosqueira & Estrada 2003; Estrada et al. 2009), which consists of a compact heavy

component and a wide-spread less massive one. The two components are produced by the difference of specific angular momentum of inflow gas, and the difference corresponds to whether gap along the planet orbit exists or not. The difference of the observed moment of inertia of Ganymede and Callisto was tried to be explained by the large difference of surface density between the two components.

The structure of a circumplanetary disk have been studied by hydrodynamic simulations. There are pioneering works that tried to see circumplanetary disks (Miki 1982; Sekiya et al. 1987; Korycansky & Papaloizou 1996), and as computational speed became faster, the structure of the circumplanetary disk became clearer by two-dimensional simulations (Kley 1999; Lubow et al. 1999; Tanigawa & Watanabe 2002) with nested-grid method (D'Angelo et al. 2002) and three-dimensional simulations (D'Angelo et al. 2003; Bate et al. 2003; Klahr & Kley 2006). In particular, recent simulations have revealed the circumplanetary disk structure and the accretion flow onto the disk in very high resolution with some special techniques, such as nested-grid methods in Eulerian codes (Machida et al. 2008, 2010; Paardekooper & Mellema 2008; Tanigawa et al. 2012; Gressel et al. 2013; Szulagyi et al. 2014) or SPH methods (Ayliffe & Bate 2009), in addition to the recent development of high-performance computers.

However, satellites around the giant planets are made of solid, and supply of solid material into circumplanetary disks have not been studied so far. There are some studies that considered accretion of particles onto giant planets under the influence of gas flow in protoplanetary disks for dust- or boulder-size particles (Rice et al. 2006;

Paardekooper 2007; Ayliffe et al. 2012; Zhu et al. 2012) or planetesimals (Zhou and Lin 2007; Shiraishi & Ida 2008), but the structure of gas flow near the planet, such as circumplanetary disks, was not resolved in such studies. In the phase of giant planet growth, circumplanetary disks are rotating around the planet almost in Keplerian velocity, and the density would be much higher than that in protoplanetary disks (Ayliffe & Bate 2009; Tanigawa et al. 2012). The particle motion is thus expected to be affected significantly by the circumplanetary disks when they are captured, and high-resolution structure of the gas flow near the planet is therefore necessary to be considered.

In this study, we examine the supply of solid material onto the circumplanetary disk by simulating motion of particles that are originally rotating in heliocentric orbits. In §2, we will explain formulation of our model, in §3 results of orbital simulation will be shown, and we discuss issues that we do not address in this paper and that might be important, and summarize our results in §5.

2. METHODS

We consider a growing giant planet embedded in a protoplanetary disk. In the disk, particles in heliocentric orbits are rotating in the protoplanetary disk. In this study, we simulate the particle motion whether the particle are captured by the circumplanetary disk under the influence of gas accretion flow onto the giant planet. We consider that the planet is rotating in a circular orbit with no inclination from the midplane of the protoplanetary disk.

2.1. Basic equations

In order to investigate the orbits of particles around the planets in detail, we use Hill's equation (e.g., Henon & Petit 1986; Nakazawa & Ida 1988) with a gas drag term. Hill's equation describes motion of small particles near a planet that is rotating around the central star, and adopts a frame rotating with a planet that is static at the origin of the coordinate on the frame. Hill's equation is usually normalized by Hill's radius for length, inverse of orbital angular velocity of the planet for time. The non-dimensional equation of the particles on the Hill coordinate can be written as

$$\frac{d\tilde{\mathbf{v}}}{d\tilde{t}} = -\nabla\tilde{\Phi} - 2\mathbf{e}_z \times \tilde{\mathbf{v}} + \tilde{\mathbf{a}}_{\text{drag}}, \quad (1)$$

where \mathbf{e}_z is unit vector in z -direction, $\tilde{\mathbf{v}}$ is velocity, \tilde{t} is time. The second term in the right-hand side is Coriolis force, which arises from the frame is rotating with the planet orbital motion. Normalized Hill potential $\tilde{\Phi}$ is given by

$$\tilde{\Phi} = -\frac{3}{\tilde{r}} - \frac{3}{2}\tilde{x}^2 + \frac{1}{2}\tilde{z}^2 + \frac{9}{2}, \quad (2)$$

where $\tilde{r} = \sqrt{\tilde{x}^2 + \tilde{y}^2 + \tilde{z}^2}$. The first term in the right-hand side corresponds to the planet potential, the second and third term describe tidal potential in horizontal and vertical direction, respectively. The last constant term is added so that potential at the Lagrange points 1 and 2 becomes zero. The acceleration due to gas drag $\tilde{\mathbf{a}}_{\text{drag}}$ is

described by

$$\tilde{\mathbf{a}}_{\text{drag}} \equiv \frac{\mathbf{F}_{\text{drag}}/m}{r_{\text{H}}\Omega_{\text{K}}^2} = -\frac{3}{8}C_{\text{D}}\frac{\rho_{\text{g}}}{\rho_{\text{s}}}\tilde{r}_{\text{s}}^{-1}\Delta\tilde{\mathbf{u}}\Delta\tilde{\mathbf{u}}, \quad (3)$$

where $\mathbf{F}_{\text{drag}} = (C_{\text{D}}/2)\pi r_{\text{s}}^2\rho_{\text{g}}\Delta\mathbf{u}\Delta\mathbf{u}$ is the drag force for a particle with radius r_{s} , m is the mass of the particle, C_{D} is non-dimensional gas drag coefficient, ρ_{g} is gas density, ρ_{s} and \tilde{r}_{s} are the internal density and the normalized physical radius of the particles, and $\Delta\mathbf{u}$ is the velocity of the objects relative to the gas. Variables with tildes denote non-dimensional quantities.

2.2. Effect of gas flow

2.2.1. Hydrodynamic simulation

We use the gas flow that was obtained by Tanigawa et al. (2012). In order to obtain gas flow with high resolution near the planet, they employed a three-dimensional hydrodynamic simulation with a nested grid code (Machida et al. 2005), which was originally developed to explore the star formation process by a collapse of the molecular cloud core (Matsumoto & Hanawa 2003). The nested grid technique enables them to obtain very high resolution gas flow in the vicinity of the planet. In the calculation they used 11 levels for nested grid. They adopted Hill's coordinate, which also contributes to enhance resolution near the planet.

In their simulation, the ratio of Hill's radius to scale height of the protoplanetary disk, which is the only one parameter of the system, was adopted to be unity. This corresponds to $M_{\text{p}} \sim 120M_{\text{E}}(a/5.2\text{AU})^{3/4}$ for $T = 280(a/1\text{AU})^{-1/2}\text{K}$, where M_{E} is Earth mass and a is semi-major axis of the planet. The planet is assumed to be in the active gas accretion phase, which corresponds to the stage after the onset of nucleated instability (Mizuno 1980; Bodenheimer & Pollack 1986; Ikoma et al. 2000), but not to be embedded in a very deep gap.

2.2.2. Background gas flow

Fig. 1 shows gas density and velocity field of the flow at the midplane. In Fig. 1a that showing wide field flow mainly focusing on outside the Hill sphere, we can see two-arm shock structure from the Hill sphere of the planet. The shock structure corresponds to spiral structure propagating in global (protoplanetary) disks. Fig. 1b shows the same flow but enlarged view focusing around the Hill sphere. We can see that there are shocks along the lines through $(\tilde{x}, \tilde{y}) \sim (\pm 1.5, 0)$ and $(0, \pm 1.5)$, where gas has discontinuity in velocity and density. Gas inside the Hill sphere shows prograde rotation. Fig. 1c shows even enlarged view. In this scale (~ 0.1 scale height), we can see another two-arm spiral structure around the planet, but the non-axisymmetric structure disappears in even smaller scale (~ 0.01 scale height) as in Fig. 1d. Note that low density region ($\tilde{r} \lesssim 0.005$) arises from sink condition around the origin (see Tanigawa et al. (2012) in detail).

2.2.3. Gas drag coefficient

The gas drag coefficient C_{D} we adopt is an approximated formula written in the form (Watanabe & Ida

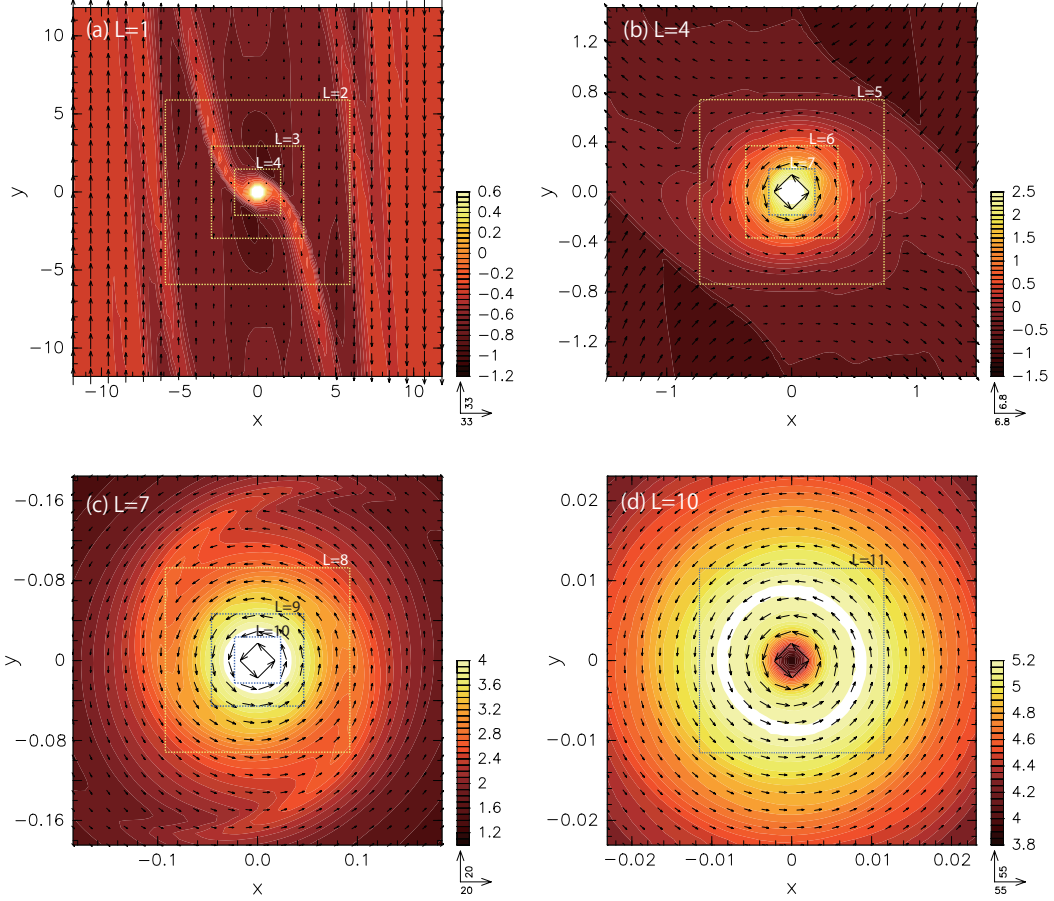


Figure 1. Velocity (arrows) and log density (color) of the flow around the planet on the midplane with four different nested level: $l = 1, 4, 7, 10$, where difference of three in level means 8 ($= 2^3$) times difference in spatial scale. Length of arrows are normalized by the two arrows in the right bottom of the each panel. Low density region near the origin ($\tilde{r} \lesssim 0.005$) mainly arises from sink treatment around the origin.

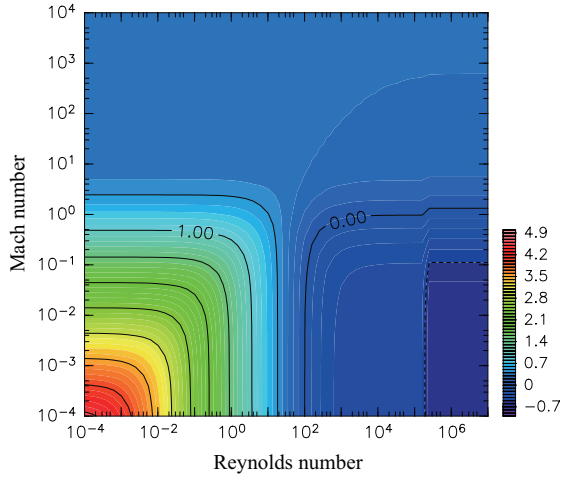


Figure 2. Log of gas drag coefficient C_D (Eq. 4) as a function of the Reynolds number and the Mach number.

1997):

$$C_D \simeq \left[\left(\frac{24}{\mathcal{R}} + \frac{40}{10 + \mathcal{R}} \right)^{-1} + 0.23\mathcal{M} \right]^{-1} + \frac{(2.0 - w)\mathcal{M}}{1.6 + \mathcal{M}} + w, \quad (4)$$

where the Reynolds number $\mathcal{R} = 2r_s u / \nu$, the Mach number $\mathcal{M} = u / c$, and w is a correction factor depending on the Reynolds number; $w = 0.4 (\mathcal{R} < 2 \times 10^5)$ and $w = 0.2 (\mathcal{R} > 2 \times 10^5)$. Relative velocity between gas and particles is u , c is isothermal sound speed, ν is kinetic viscosity $\nu = 0.353 \sqrt{8/\pi} c \ell_g$ (Champman & Cowling 1970), ℓ_g is mean free path¹. Fig. 2 shows the value of C_D as a function of the Mach number and the Reynolds number.

As in Eq. (4), C_D is a function of the two non-dimensional numbers: the Mach number and the Reynolds number. However we need the ratio of the particle size to mean free path of molecules when we evaluate the Reynolds number. Thus we convert the result of hydrodynamic simulation, which is obtained in non-dimensional form, into quantities with real dimensions. To do that, we adopt a disk model for gas temperature $T = 280\text{K}(a/1\text{AU})^{-1/2}$ and gas surface density $\Sigma_g = 1.7 \times 10^4 f_H \text{ kg/m}^2 (a/1\text{AU})^{-3/2}$, where f_H is scaling factor relative to that of the minimum mass disk model (Hayashi 1985). We adopt $\sigma_{\text{mol}} = 2.0 \times 10^{-19} \text{ m}^2$ and $m_{\text{mol}} = 3.9 \times 10^{-27} \text{ kg}$. We fixed $a = 5.2 \text{ AU}$ in this paper

¹ We define mean free path as $\ell_g = m_{\text{mol}} / (\sigma_{\text{mol}} \rho_g)$, where m_{mol} and σ_{mol} are mass and collision cross section of molecule, whereas Champman & Cowling (1970) defined it as $\ell_g = m_{\text{mol}} / (\sqrt{2} \sigma_{\text{mol}} \rho_g)$, which makes apparent difference of the coefficients in the formulae of viscosity.

and fiducial value for f_H is 1.

2.3. Numerical method

We integrate Eq. (1) for particles with wide range of size, using the Runge-Kutta-Fehlberg method with adaptive step size (e.g., Press et al. 2007). We consider a two-dimensional problem; the orbits of particles is in the same plane of the planet orbit and the midplane of the protoplanetary disk. We also restrict ourselves to initially zero-eccentricity particles. Because of these simplification, we only have one parameter; impact parameter \tilde{b} , which is defined as the value of x coordinate of the particle position at $\tilde{y} \rightarrow \infty$. In numerical simulation, we cannot set infinite \tilde{y} as an initial position of the particles, thus we set the initial position $(\tilde{x}_0, \tilde{y}_0)$ where $\tilde{x}_0^2 = \tilde{b}^2 - 8/\tilde{y}_0$, which is valid when $\tilde{x}_0 \ll \tilde{y}_0$ (Ida & Nakazawa 1989; Ohtsuki 1999). We set $\tilde{y}_0 = 100$ and \tilde{x}_0 is less than 3, so the double inequalities are met in our case.

The termination conditions of the orbital integration are follows: (1) Collision with the planet. We terminate numerical integration when $\tilde{r} < \tilde{r}_p$ where \tilde{r}_p is physical size of the planet in our unit. We set $\tilde{r}_p = 0.001$, which roughly corresponds to the physical size of a planet at 5AU. In the gas-free case case, results depends on the size of the planet, but we mainly focus on the case where particles are captured by the circumplanetary disks, not by the planet, so the physical size of the planet is not important in this work as long as the size is small enough. (2) Receding from the planet: $|\tilde{y}| > \tilde{y}_0$. These particles first approach at least about a few Hill's radii and then move away from the planet without collision with the planet or captured by the circumplanetary disk.

As described above, the particles are assumed to be on the midplane of the protoplanetary disk and initially in a circular orbit around the central star. We consider wide range of particle size, so this assumption would not be always valid, but particles in a size range in which accretion to the circumplanetary disk is effective (see Section 3) can be considered to be settled down toward the midplane even when we consider stirring up of particles by turbulence. The thickness of the solid particles h_d is given by (Okuzumi et al. 2012; Youdin & Lithwick 2007)

$$h_d = h \left(1 + \frac{\Omega t_s}{\alpha} \frac{1 + 2\Omega t_s}{1 + \Omega t_s} \right)^{-1/2} \quad (5)$$

where Ω is angular velocity of Keplerian rotation around the central star, α is non-dimensional turbulent viscous parameter (Shakura & Sunyaev 1973), t_s is stopping time of particles. If we assume $\alpha \sim 10^{-2}$, thickness of 1m-sized particles layer is 1/10 of scale height of the gas disk at 5AU, and the typical size for effective accretion is roughly larger than 1 meter, as we will see, so the two-dimensional approximation is reasonable. Once particles are in a thin layer, inclination cannot be pumped up by gravitational scattering. On the other hand, eccentricity is easier to be enhanced by the planet gravity (Ida 1990; Ohtsuki et al. 2002). If synodic period is longer than the stopping time, the assumption of circular orbit should be valid because eccentricity would be damped until the next approach by Keplerian shear. This condition roughly corresponds to the size $r_s \lesssim 100$ m. Particles with sizes larger than ~ 100 m, however, would have

some eccentricity comparable to the order of unity when they approach the planet, which would affect the result. Although we should keep this in mind, we assume circular orbit for the initial condition of the particles for simplicity.

3. RESULTS

3.1. Typical orbits of captured particles

3.1.1. Strong gas drag case: Orbits of small particles

We first describe particle motion in the case of strong gas drag, which corresponds to particles with size roughly smaller than 1m. Fig. 3 shows orbits of small particles ($r_s \leq 10$ m) around the Hill sphere. Fig. 3a shows orbits of 1cm-sized, which is almost the same as streamline of gas because gas and particles are well coupled. Gas in the region $\tilde{x} > 0$ approaches with Keplerian shear motion in negative y direction from large \tilde{y} region. For gas that closes with the Hill sphere passes the shock surface that enhances density and reduces velocity. Gas that reaches at about $(\tilde{x}, \tilde{y}) \sim (1.0, 0.5)$ bifurcates toward two streams in front of the Hill sphere; one crosses the y -axis (the planet orbit), makes U-turn, and goes back to positive y direction. The other stream passes by the Hill sphere without crossing y -axis and moves towards negative y direction (see Fig. 1 and also Tanigawa et al. (2012) in detail). Since gas in the midplane does not accrete onto the circumplanetary disk, 1cm particles do not either. For 10cm-sized particles (Fig. 3b), overall orbits outside the Hill sphere looks very similar to that of 1cm-sized case, but one clear difference is that there are orbits that enters the Hill sphere and accretes into the circumplanetary disk, although gas does not enter it through the midplane. This is because, although the particles are well coupled with gas in the Keplerian timescale, the particles just after the shock surface tend to decouple with gas in a short timescale, which leads to the deviation of the orbit from gas motion. Near the bifurcation point of the gas flow and in front of the shock surface, the motion of the particles is directed toward the planet, which enable the particles to intrude into the Hill sphere against the drag of gas that is not going to enter. This feature becomes more significant for larger particles. In the case of 1m-sized particles (Fig. 3c), there is wider band in which the particles are accreting onto the circumplanetary disk. This means that the deviation of the particle motion from the gas flow is more significant especially after the shock surface. In addition, we can see orbits that cross with each other, which does not occur in the case of smaller particles. This is one of typical behaviors of motion for decoupled particles. In the case of particles with 10m (Fig. 3d), the motion outside the Hill sphere is almost free from gas drag, but if the particles go into the Hill sphere and get closer to the planet, the particles are captured by the denser gas of the circumplanetary disk at the deeper region. Note that there is an orbit that looks like deflected at $(x, y) \simeq (0.2, 1.0)$ is an apparent motion on the rotating frame. The particle are actually rotating smoothly on the inertial frame even around the apparent deflected point, but the Hill coordinate are rotating with the Keplerian angular velocity of the planet orbital motion, and the rotating velocity is subtracted on the Hill coordinate. Thus the orbit looks like deflected. This feature is notable where the distance

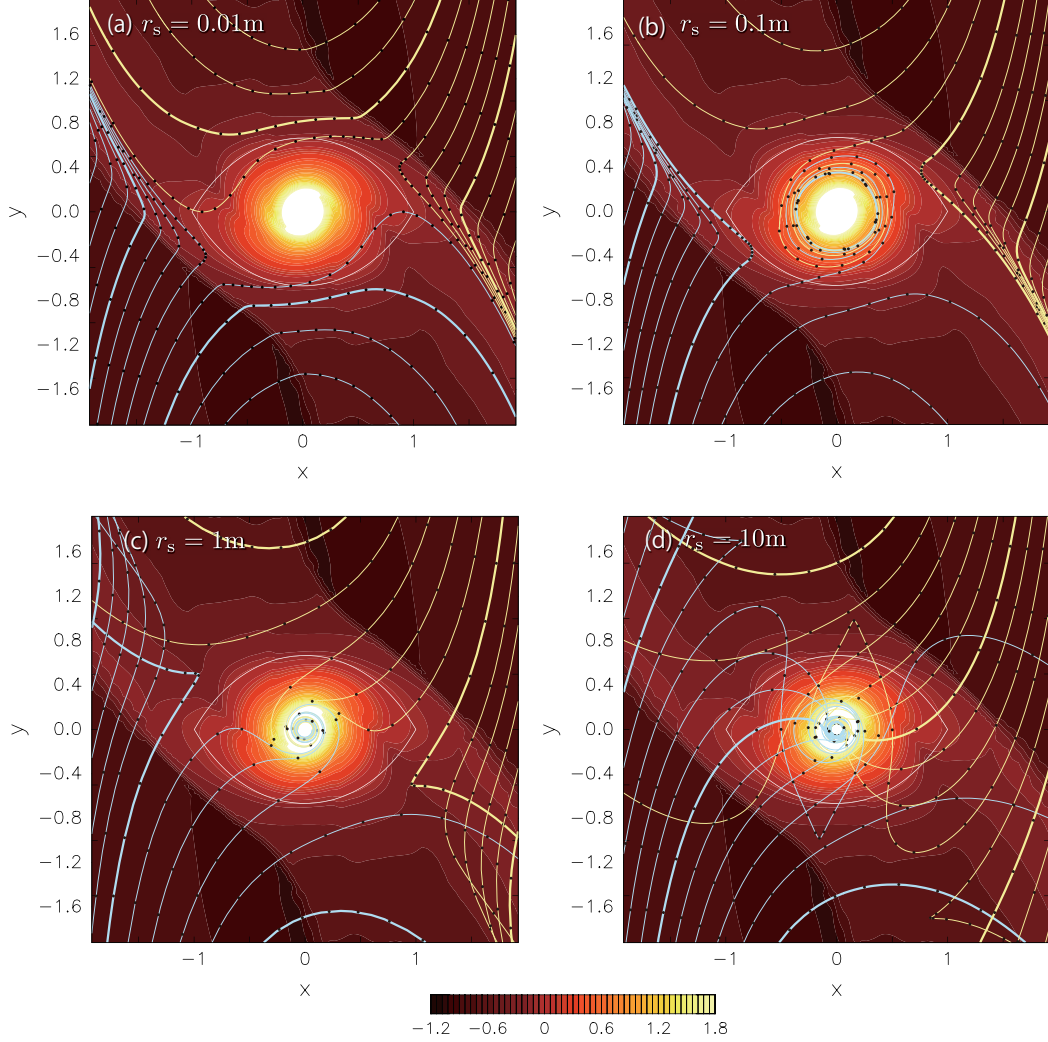


Figure 3. Orbits of particles with size $r_s = 10^{-2}\text{m}$ 10^{-1}m , 10^0m , 10m . Background colors show \log_{10} of gas density, and yellow and blue lines show orbits of the particles. Black dots on the orbits are put every 0.2 unit time. White line shows the Hill sphere.

from the planet is near the Hill radius because, in that region, the Keplerian angular velocity around the planet is close to that around the central star.

3.1.2. Weak gas drag case: Orbits of large particles

Next we describe particle motion in the case of weaker gas drag, which corresponds to particles with size roughly larger than 1m , although the size ranges for the two cases (strong and weak gas drag cases) overlap with each other, which promotes a deeper understanding of the capturing process. Before showing orbits of the particles, we introduce minimum distance to the planet of an orbit as a function of impact parameter \tilde{b} in the gas free case. Fig. 4 shows minimum distance between particles from the planet through the orbits for gas-free case, which was presented by Petit & Henon (1986); Ida & Nakazawa (1989). The distance is referred to as $\tilde{r}_{\text{min,free}}$ in this paper. There are two main collisional bands (Giuli 1968), which divide encounter type into three in terms of encounter direction; $\tilde{b} \lesssim 2.1$, $2.1 \lesssim \tilde{b} \lesssim 2.4$, and $\tilde{b} \gtrsim 2.4$, which correspond respectively to prograde, retrograde, and prograde encounters. We can expect that, in the retrograde encounter regime,

particles tend to get strong gas drag and are easy to be captured, while particles in the prograde encounter regimes are more difficult to be captured. Note that there are very narrow bands which show close encounter in a discontinuity manner with respect to \tilde{b} , which arises from multiple encounter in each orbit (e.g., Nishida 1983; Ida & Nakazawa 1989). But this is so narrow that the bands does not have any significant effect on the solid accretion rate onto the circumplanetary disk in a statistical sense.

Fig. 5 shows example orbits in prograde capturing regime. We show orbits of several particle sizes in the case with $\tilde{b} = 2.022$, in addition to the gas-free case which corresponds to the orbit of $\tilde{r}_{\text{min}} = 0.0250$ (see also Fig. 4). Fig. 5a shows orbits in wide area focusing on how particles approach the Hill sphere from heliocentric orbits. We cannot see any significant difference between the three cases until they reach the Hill sphere including the gas-free case. Fig. 5b shows close-up view of Fig. 5a. We can see that the particle of 10cm size does not enter the Hill sphere and recedes from it. This is because the particle is well coupled with gas, as mentioned before. For the 1m -sized particle, it can penetrate

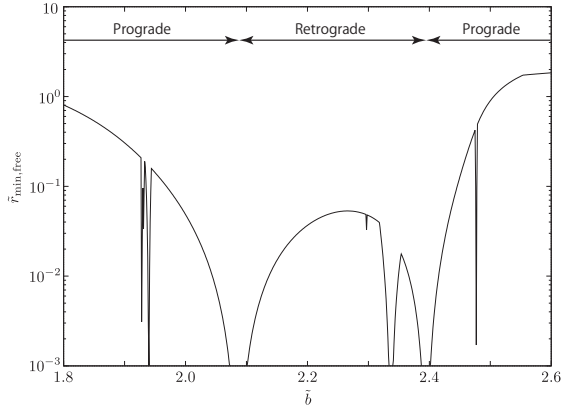


Figure 4. Minimum distance to the planet of particles with initially circular and no inclination orbits as a function of impact parameter \bar{b} in the gas-free case ($\tilde{r}_{\min, \text{free}}$). In the regions $\bar{b} \lesssim 2.1$ and $\bar{b} \gtrsim 2.4$, particles encounter the planet in prograde direction, while $2.1 \lesssim \bar{b} \lesssim 2.4$ particles encounter it in retrograde direction.

into the Hill sphere through the low velocity gas at the post shock region. Although the deviation of the orbit from the gas flow is sensible for the intruding motion, the particle still get significant effect from the gas that rotates prograde direction, thus the particle starts rotating also in the same direction. Fig. 5c shows more close-up view of orbits of other three different sizes (1m, 100m, 10000m). In the case of 1m size, we can see that the particle gradually spirals into inner region. In the case of 100m size, the particle motion is almost the same as that of gas-free case until distance from the planet becomes less than about 0.2. But after the first encounter at $(\tilde{x}, \tilde{y}) = (-0.05, 0)$, the particle is immediately circularized in a few orbit around the planet. Once the orbit is circularized, the orbit does not change because the gas motion in this region is almost circular, which results in weak gas drag force. In the case of 10000m size, the particle moves along with the orbit of gas-free case even around the first encounter, but the particle is captured in the Hill sphere because of energy dissipation by the gas drag through the first encounter, and the orbit becomes highly eccentric. Since the gas drag is not so effective in comparison with smaller particle cases, it takes longer time to be circularized. In the course of the circularization, the distance of apocenter continuously decreases whereas the pericenter does not change significantly.

Fig. 6 shows orbits of particles in the retrograde encounter regime ($\bar{b} = 2.174$) with several-size particles as well as the gas-free case. The distance at the closest approach for the gas-free case is $\tilde{r}_{\min} = 0.0253$, which is similar to that of the prograde case of $\bar{b} = 2.022$ shown in the above. Fig. 6a shows orbits in the wide field. For the gas-free case, the particle enters the Hill sphere and encounters with the planet, then escapes from the Hill sphere. For the small particles ($r_s = 1\text{m}$), the motion of approaching the Hill sphere is similar to that of the gas-free case, but they cannot enter the Hill sphere because of the strong gas drag with the gas that does not enter the Hill sphere, which can also be observed in the prograde case. Figs. 6b and c show close-up views of orbits. Unlike the 1m case, 10m and larger particles can enter the Hill sphere across the high-density low-velocity region after the shock surface. However, the motion of

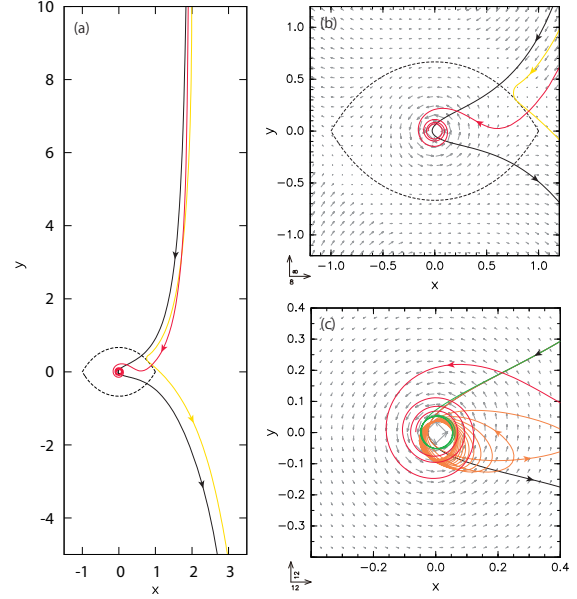


Figure 5. Orbits of particles of $\bar{b} = 2.022$, which corresponds to prograde encounter region. Left and right upper panels shows orbits of particles in the case with $r_s = 0.1\text{m}$ (yellow), 1m (red), and gas-free (black), respectively. Right lower panel shows $r_s = 1\text{m}$ (red), 100m (green), 10000m (Orange) cases. Vectors in the middle and right panels shows velocity field of the gas flow.

10m-sized particle is strongly affected at $\tilde{r} \lesssim 0.2$ by the motion of the gas that is in prograde rotation. Thus the 10-sized particle, which was originally moving in retrograde direction, flips the direction to prograde, and rotates in almost circular orbit in accordance with the motion of the circumplanetary disk. The spiral-in motion is due to the drag from the gas, which is rotating in sub-Keplerian velocity. In the case of larger particles (100m and 1000m), the tendency is similar. But the effect of the gas drag becomes weaker, so the point of turn-over to prograde becomes closer to the planet. For both cases, the particles settle in circular orbits, and the orbital radius of circularization decreases with increasing particle size. The deviation from true circles (inward spiral movement) is less significant compare to that of the 10m case. However, in the case of the 10000m-sized particle, the gas drag is so weak that the particle cannot change the direction from retrograde to prograde in the course of the approach to the planet, and falls to the planet before circularization or change the direction in accord with gas flow.

3.2. Capture radius in circumplanetary disks

In order to consider processes of satellite formation in a circumplanetary disk, we need to know where solid particles are supplied at the circumplanetary disk. As we showed in the previous section, the captured particles eventually become circular orbits in the prograde direction in a short timescale unless the particles collide with the planet before being circularized. Since the relative velocity with the gas after the circularization is very small, the timescale of orbital evolution due to gas drag becomes much longer than that of the circularization. We therefore define the captured radius as a distance from the planet at the circularization, which is different from the normal definition of capture in an energetic

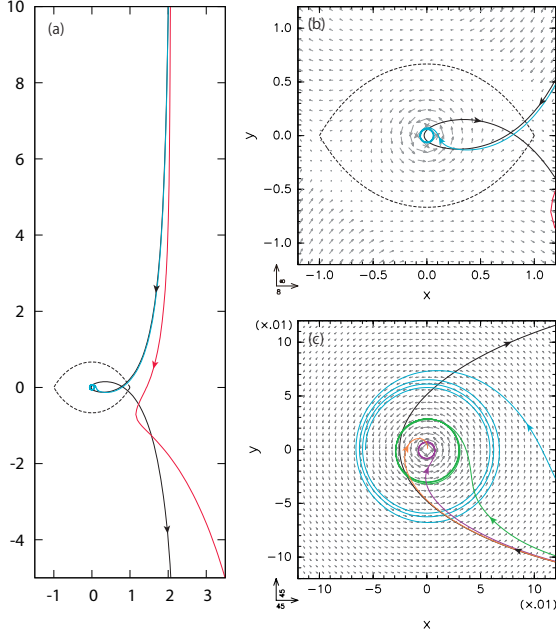


Figure 6. Orbits of particles of $\tilde{b} = 2.174$, which corresponds to retrograde encounter region. Left and right upper panels show $r_s = 1\text{m}$ (red), 10m (blue), and gas free (black) cases. Right lower panel shows $r_s = 10\text{m}$ (blue), 100m (green), 1000m (purple), 10000m (orange) and gas-free cases. Vectors in the right panels show velocity field of the gas flow.

sense; Jacobi energy $\tilde{E}_J = \tilde{v}^2/2 + \tilde{\Phi}$ becomes negative. More specifically, we define the captured radius at the time when either of the two condition is met: (1) Circularized in the circumplanetary disk: $\tilde{E}_J < 0$ and $e < 0.3$ and $\tilde{a} < 0.5$ and $N_w \geq 3$, where e and \tilde{a} are eccentricity and semi-major axis of the particle around the planet, and N_w is winding number (Kary & Dones 1996; Iwasaki & Ohtsuki 2007). When a particle crosses the x - or y -axis in the prograde direction around the planet, $1/4$ is added to N_w , while the same amount is subtracted from N_w when it crosses the axes in the retrograde direction. (2) Winded capture: $\tilde{E}_J < 0$, and $N_w \geq 15$. When one of the above conditions is met, the captured radius \tilde{r}_{cap} is determined as the larger one of the two: pericenter of the orbit at the time when the condition is met, or the minimum distance from the planet until the time when the condition is met. We define \tilde{r}_{cap} as the larger one of \tilde{a} or \tilde{r}_{min} when either of the two conditions are met, and we do not define it when neither of the two are met. The former condition (1) is mainly for the weak gas-drag cases where the orbit is gradually shifting toward circular from highly eccentric orbit. The latter (2) is for the strong gas-drag cases where osculating Keplerian orbital elements are difficult to determine. Note that there are adjustable parameters to determine the captured radius, but the result is not sensitive to the parameters.

Fig. 7 shows the captured radius as a function of \tilde{b} . In the case of $r_s = 0.1\text{m}$, the particles with impact parameter between $\tilde{b} \simeq 1.9$ and 2.0 are captured, and particles in all the other regime basically do not enter the Hill sphere (see Fig. 3), which is totally different behavior from the gas-free case (green dotted line). The position of the captured band is different from either of the two collision bands of the gas-free case, which reflects the fact

that the motion is strongly affected by the gas flow before approaching the Hill sphere. In the case of $r_s = 1\text{m}$, captured band becomes wider in comparison with the 0.1m case because the particles are easier to penetrate into the Hill sphere through the lower-velocity higher-density region at the post shock (see Figs. 1 and 3). The captured radius is smaller than that of the 0.1m case since, to be captured by the circumplanetary disk, larger particles need higher density of gas and the gas density in the circumplanetary disk increases with decreasing distance from the planet.

In the cases of $r_s = 10\text{m}$, 100m , 1000m , they show similar behavior with some quantitative differences. In this size regime, the particles are basically decoupled from the gas flow at the outside of the Hill sphere, which are confirmed by the fact that the minimum distance from the planet outside the captured band matches well with that of the gas-free case (see red and green lines in Fig. 7). Width of the captured band slightly decreases with increasing particle size, which reflects that the effect of the gas drag for capture becomes more effective at the region closer to the planet where gas density and relative velocity is generally higher. There is a flat region at the bottom of \tilde{r}_{cap} for each panel. We define the radius of the flat region as critical radius for capture $\tilde{r}_{\text{cap,crit}}$. Once particles enter inside the radius, gas drag is so strong that the particles are forced to move with the gas flow of the circumplanetary disk regardless of orbits before they reach the radius. The typical cases for this kind of capture can be seen in the retrograde encounter region (see Fig. 6); all the particles in the retrograde encounter region are captured by the circumplanetary disk. But, in both edges of the captured band, we can see captured region where $\tilde{r}_{\text{min,free}}$ is larger than the critical radius. In this region, the particle is first captured energetically (i.e., $\tilde{E}_J < 0$) in a highly eccentric orbit with the pericenter around $\tilde{r}_{\text{min,free}}$, and then circularized. During the circularization process, the particles tend to keep the pericenter, thus \tilde{r}_{cap} is roughly aligned with $\tilde{r}_{\text{min,free}}$ in this regime.

In the cases of $r_s = 100\text{m}$ and 1000m , there is a band where $\tilde{r}_{\text{cap}} < \tilde{r}_{\text{min,free}}$ around $\tilde{b} \sim 2.2 - 2.3$. The particles in this region approach the planet in the retrograde direction, thus the particles cannot pass through near the $\tilde{r}_{\text{min,free}}$ as a pericenter and cannot make an elliptic orbit like that occurred in the two edge regions. Instead, the particles are forced to change the direction into prograde and rotate with disk gas that is rotating in almost Keplerian motion.

In the case of $r_s = 10000\text{m}$, there is no flat and base region for \tilde{r}_{cap} because the critical radius for capture is smaller than the planet physical radius, which means the particles collide with the planet. In other words, the gas drag is not strong enough to change the direction from retrograde to prograde in the course of approaching the planet.

In order to understand the capturing processes more deeply, we study particle-size dependence of captured radius. Since the capture radius is a function of \tilde{b} even for single size particles as seen in Fig. 7, we introduce critical radius for capture $\tilde{r}_{\text{cap,crit}}$ as a typical capture radius for a given size regardless of \tilde{b} so that we do not need to consider the detail of the \tilde{b} dependence. We

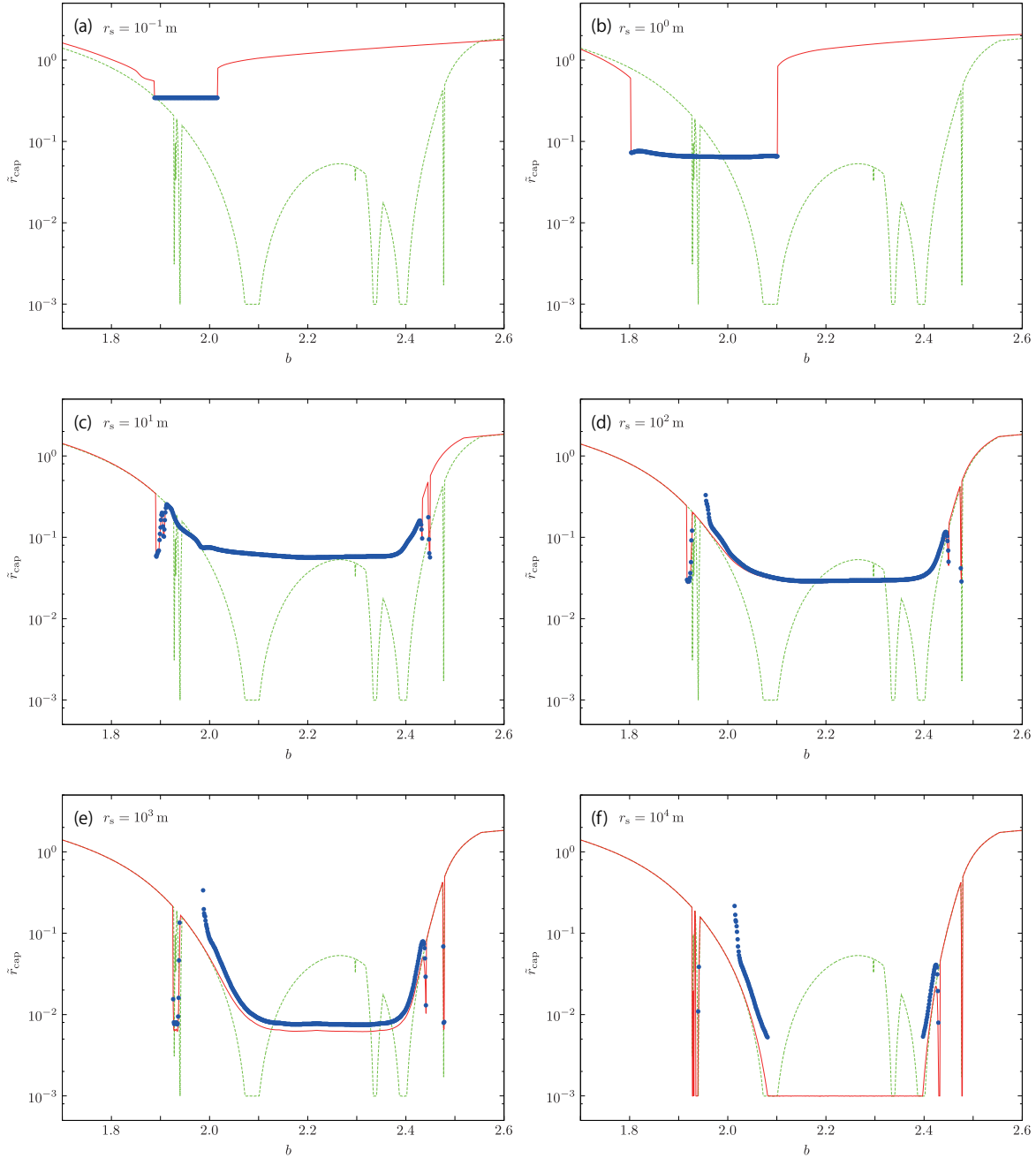


Figure 7. Captured radius \tilde{r}_{cap} (blue) and minimum distance from the planet until the particles are judged as captured by the circumplanetary disk, collision with the planet, or recede enough from the Hill sphere after encounters (red, see §3.2) as a function of \tilde{b} for a wide range of particle size ($r_s = 0.1\text{m}, 1\text{m}, 10\text{m}, 100\text{m}, 1000\text{m}, 10000\text{m}$). Green curves show $\tilde{r}_{\text{min,free}}$, which is the minimum distance from the planet in the gas-free case.

define $\tilde{r}_{\text{cap,crit}}$ by the radius where captured radius \tilde{r}_{cap} (blue dots in Fig. 7) shows wide and flat region at the bottom of \tilde{r}_{cap} as seen in Fig. 7 a-e. In order to define $\tilde{r}_{\text{cap,crit}}$, we introduce two other radii $\tilde{r}_{\text{cap},1/4}$ and $\tilde{r}_{\text{cap},1/2}$; $\tilde{r}_{\text{cap},1/4}$ is defined so that the number of captured particles with $\tilde{r}_{\text{cap}} < \tilde{r}_{\text{cap},1/4}$ account for 1/4 of all the captured particles under the condition of uniform interval in \tilde{b} , and $\tilde{r}_{\text{cap},1/2}$ is defined in the same way. The width of the bottom region is roughly half of the whole captured band, thus we define $\tilde{r}_{\text{cap,crit}} = \tilde{r}_{\text{cap},1/4}$ when $\tilde{r}_{\text{cap},1/4} \simeq \tilde{r}_{\text{cap},1/2}$. If the difference is large, for example $\tilde{r}_{\text{cap},1/2}/\tilde{r}_{\text{cap},1/4} > 1.1$, the $\tilde{r}_{\text{cap,crit}}$ is smaller than \tilde{r}_p ,

and many particles are collides with the planet, as seen in Fig. 7f and we do not define $\tilde{r}_{\text{min,crit}}$.

Fig. 8 shows normalized capture radii $\tilde{r}_{\text{cap},1/4}$ and $\tilde{r}_{\text{cap},1/2}$ in the cases with three different scaling factors of gas surface density $f_H = 1, 10^{-2}, 10^{-4}$ (see § 2.2.3). First we can clearly see the tendency that both of the two radii decrease with increasing particle size, which is observed in Fig. 7. We can also see that the difference of the two is small when the radii are larger than 10^{-2} . In this regime, $\tilde{r}_{\text{cap,crit}}$ can be well defined by $\tilde{r}_{\text{cap},1/4}$. Note that the main reason why the difference between the two radii become large at $\tilde{r}_{\text{cap}} \lesssim 10^{-2}$ is the artificial effect of

the background flow; gas density at the midplane of the circumplanetary disk in $\tilde{r}_{\text{cap}} \lesssim 10^{-2}$ tends to be smaller because of sink treatment near the origin in the hydrodynamic simulation, in which the gas drag effect would be underestimated.

The decrease of gas density (i.e., f_H) basically makes the lines shift toward the left in the figure, because particles have to go deeper denser region to be captured when whole gas density is uniformly smaller. Decrease of f_H , which corresponds to gas depletion of the protoplanetary disk due to gap formation around the planet orbit or global disk dissipation, basically makes the lines shift toward the left in the figure, because particles have to go deeper denser region to be captured when whole gas density is uniformly smaller.

Note however that this is not a simple linear dependence because the gas drag coefficient C_D is generally not a simple power-law function of the Reynolds number and the Mach number (Adachi et al. 1976), and the coefficient we use is not either (see §2.2.3). In particular, in the case of high surface density ($f_H = 1$), gas drag law can be Stokes regime where drag force is independent of gas density, which can change the tendency, and which is reflected on the jaggy curve of the case of $f_H = 1$.

We also plot fitted lines of $\tilde{r}_{\text{cap,crit}}$ in the region where $\tilde{r}_{\text{cap}} \gtrsim 10^{-2}$ given by

$$\tilde{r}_{\text{cap}} = 0.16 \left(\frac{r_s}{1\text{m}} \right)^{-0.4} \left(\frac{f_H}{1} \right)^{0.4}. \quad (6)$$

Although this is an empirical formula, the value 0.4 in the index can also be estimated by the balance between energy dissipation due to gas drag and kinetic energy of particles assuming that C_D is constant and that particle velocity is determined only by potential energy of the planet. If we assume gas density is axisymmetric and the density is described by a power-law function as $\rho_g \propto \tilde{r}^{-\gamma}$, capture radius can be analytically obtained as $\tilde{r}_{\text{cap}} \propto r_s^{1/(1-\gamma)}$, which is derived by comparison between dissipation energy through gas drag and potential energy needed to be captured by the planet gravity (see Tanigawa & Ohtsuki 2010; Fujita et al. 2013, in detail). Equating the two indexes on \tilde{r}_s , we have $\gamma = 3.5$, which is consistent with the density distribution we use (Tanigawa et al. 2012). We also show a simple mean radius with respect to \tilde{b} given by

$$\langle \tilde{r}_{\text{cap}} \rangle = \exp \left(\frac{\int_0^\infty \log(\tilde{r}_{\text{cap}}) \frac{3}{2} \tilde{b} d\tilde{b}}{\int_0^\infty \frac{3}{2} \tilde{b} d\tilde{b}} \right), \quad \text{for all the captured orbits.} \quad (7)$$

The mean radius $\langle \tilde{r}_{\text{cap}} \rangle$ also shows the similar trend of $\tilde{r}_{\text{cap},1/2}$, but since the distribution is far from symmetric about the mean value, the mean radius is not necessarily suitable to define $\tilde{r}_{\text{cap,crit}}$.

3.3. Capture rate by circumplanetary disks

Fig. 9 shows normalized probabilities of capture by the circumplanetary disk and by the planet.

We define normalized probabilities captured by the cir-

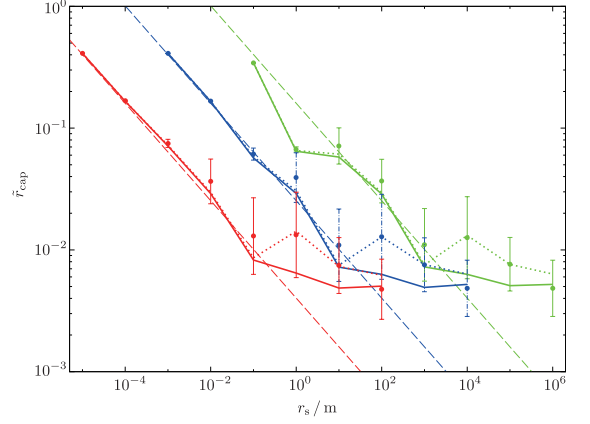


Figure 8. Normalized capture radius as a function of particle size r_s . Green, blue, and red lines show scaling (depletion) factor of gas density $f_H = 1, 10^{-2}, 10^{-4}$, respectively. Solid and dotted lines show $\tilde{r}_{\text{cap},1/4}$ and $\tilde{r}_{\text{cap},1/2}$, respectively. Filled circles show $\langle \tilde{r}_{\text{cap}} \rangle$ (mean of \tilde{r}_{cap} with respect to \tilde{b}) and error bar shows standard deviation in logarithmic space. Thin dashed lines show fitted lines given by Eq. (6).

cumplanetary disk and the planet as

$$P_{\text{disk}}(r_s, f_H) = 2 \int_0^\infty \varphi_{\text{disk}}(r_s, f_H, \tilde{b}) \frac{3}{2} \tilde{b} d\tilde{b}, \quad (8)$$

$$P_{\text{planet}}(r_s, f_H) = 2 \int_0^\infty \varphi_{\text{planet}}(r_s, f_H, \tilde{b}) \frac{3}{2} \tilde{b} d\tilde{b}, \quad (9)$$

where φ_{disk} is a judgment function whether a particle is captured by the circumplanetary disk: unity if the particle is captured, and zero otherwise. The definition of φ_{planet} is in the similar way; unity if the particle collides with the planet, and zero otherwise. Note that all the particles that are judged as capture by the circumplanetary disk is going to collide with the planet after long term inward orbital evolution by gas drag, but we use the conditions for capture described in §3.2.

Although we show three different f_H , we do not see significant qualitative difference between them, so we focus on the case of $f_H = 1$ below, unless otherwise stated. In the limit of small particle size ($r_s \leq 0.01\text{m}$), both P_{disk} and P_{planet} are zero because small particles that are well coupled with gas cannot enter into the Hill sphere. From $r_s = 0.1\text{m}$ to 10m , P_{disk} increases with r_s , which corresponds to the increase of the captured band seen in Fig. 7a-c. But P_{planet} is still zero because all the particles that enter the Hill sphere are captured by the circumplanetary disk. From $r_s = 10\text{m}$ to 1000m , P_{disk} does not change significantly because the width of the captured band weakly decrease with r_s as described in §3.2. When $r_s \geq 1000\text{m}$, P_{disk} decreases with increasing r_s . This is because gas drag become ineffective and some fraction of particles collide with the planet, rather than captured by the circumplanetary disk. In the limit of $r_s \rightarrow \infty$, we expect $P_{\text{disk}} = 0$ and $P_{\text{planet}} = 11.3\sqrt{\tilde{r}_p}$ (Ida & Nakazawa 1989; Inaba et al. 2001). In the case of our setting ($\tilde{r}_p = 10^{-3}$), we have $P_{\text{planet}} = 0.36$, in which P_{planet} is approaching with increasing r_s . Note that the reason why $P_{\text{planet}} > 0.36$ in this weak-drag regime is that gas drag enhances the collision rate onto the planet (Inaba & Ikoma 2003; Tanigawa & Ohtsuki 2010).

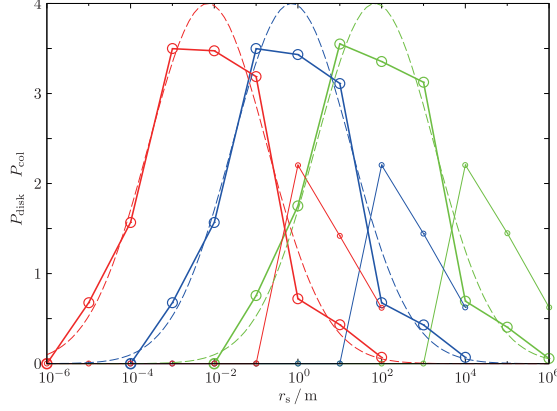


Figure 9. Normalized probability of capture by the circumplanetary disk P_{disk} (thick lines) and the planet P_{planet} (thin lines) as a function of particle size r_s . Blue, green, red lines show $f_H = 1, 10^{-2}, 10^{-4}$, respectively.

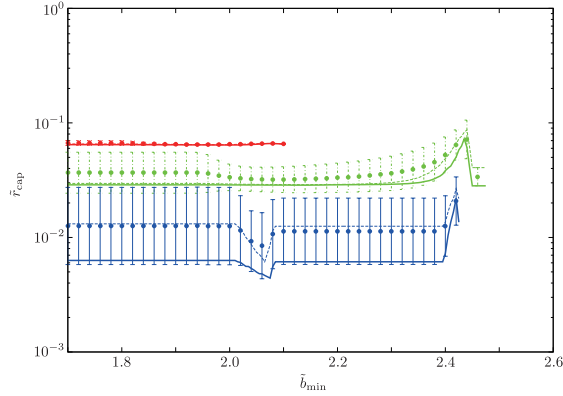


Figure 10. Dependence of mean capture radius \tilde{r}_{cap} on width of particle gap. Horizontal axis is \tilde{b}_{min} , which is the lower bound of the region where particles exist. Red, green and blue show the case with $r_s = 1, 10^2, 10^4$ m particles, respectively. Filled circles show log average and error bars show one sigma. Thick lines and thin dashed lines show $\tilde{r}_{\text{cap},1/4}$ and $\tilde{r}_{\text{cap},1/2}$, respectively.

Finally we fit P_{disk} by an formula. An empirical formula for P_{disk} can be roughly approximated as

$$P_{\text{disk}}(r_s, f_H) = \begin{cases} P_{\text{max}} \exp \left[- \left(\frac{\log(r_s/r_{s,\text{peak}})}{\log W_{s,\text{HWHM}}} \right)^2 \right] & \text{if } r_s \gtrsim 5 \times 10^{-4} r_{s,\text{peak}} \\ 0 & \text{otherwise,} \end{cases} \quad (10)$$

where $P_{\text{max}} = 4.0$, $r_{s,\text{peak}} = 70f_H$ m, $W_{s,\text{HWHM}} = 100$. The fitted lines are also plotted in Fig. 9. This formula is not derived by physical consideration, but it might be useful for rough estimation.

4. DISCUSSION

We have assumed so far that particle surface density is uniform in the protoplanetary disk before particles approach the planet, but that is not true in general. In particular, a particle gap, which is a lower surface density annular region round the planet orbit, can form easier than the gap of gas (e.g., Tanaka & Ida 1997; Paardekooper 2007; Zhou and Lin 2007; Shiraishi & Ida 2008; Ayliffe et al. 2012). We will examine the effect of

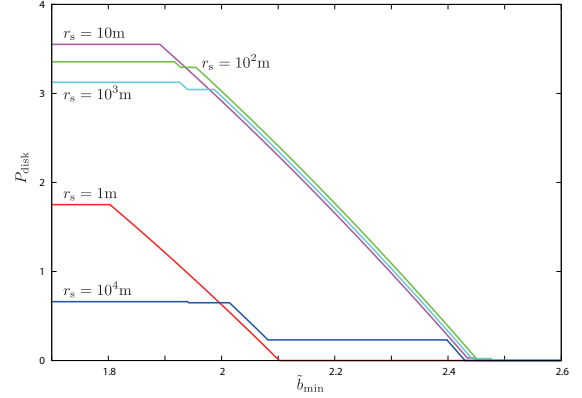


Figure 11. Dependence of normalized probability of the capture by the circumplanetary disk on the width of particle gap.

the gap opening on the accretion rate of the particles. To examine the effect, we calculate \tilde{r}_{cap} and P_{disk} as a function of gap width that we define by \tilde{b}_{min} so that particles uniformly exist at $\tilde{b} > \tilde{b}_{\text{min}}$ and there are no particles at $\tilde{b} < \tilde{b}_{\text{min}}$. Fig. 10 shows the dependence of $\tilde{r}_{\text{cap},1/2}$, $\tilde{r}_{\text{cap},1/4}$, and $\langle \tilde{r}_{\text{cap}} \rangle$ on \tilde{b}_{min} . In the case with $r_s = 1$ m, \tilde{r}_{cap} do not depend on \tilde{b}_{min} almost at all, and even when $r_s = 10^2$ and 10^4 m cases, \tilde{r}_{cap} changes only by a factor of a few. This shows that even when the particle gap is formed and particles distribution is far from uniform, there is no significant impact on capture radius.

Fig. 11 shows P_{disk} as a function of \tilde{b}_{min} for various values of r_s . In contrast to Fig. 10, we can see that P_{disk} decreases almost linearly with \tilde{b}_{min} in the region where particles are captured. This can be easily understood by Fig. 7. This simply means that when particle gap opens widely, accretion rate onto the circumplanetary disk reduces, and when $\tilde{b}_{\text{min}} \gtrsim 2.4$, no particle accretion is expected. Note that the horizontal parts of the lines indicate that non-capture regions such as $1.93 < \tilde{b} < 1.98$ in Fig. 7e or $2.09 < \tilde{b} < 2.40$ in Fig. 7f.

Muto & Inutsuka (2009) derived an analytic formula that describes radial migration of small particles near a low-mass planet embedded in a protoplanetary disk. According to Eq. (68) of their paper and comparing the two dominant terms (gravitational scattering by the planet and radial inward migration due to slight difference of rotation velocities), we obtain the gap width, which corresponds to \tilde{b}_{min} in this study, as 2.04, in the case that normalized stopping time is unity and degree of non-Keplerian rotation of disk gas (η in their notation) is 10^{-3} . This would mean that particle gap is still narrow enough for particles to accrete onto circumplanetary disks (see Fig. 11). Note however that we extrapolate their formula beyond their assumption (i.e., they do not consider large density change, such as gap formation of gas disk), which would probably change the estimation here.

Although gap structure of gas would create a particle gap and dam radial flow of particles toward the planet, particles in a particular size range can pass through the gap and be able to approach the planet (Rice et al. 2006; Paardekooper 2007; Ward 2009; Morbidelli & Nesvorniy 2012; Zhu et al. 2012). Also, strong pressure gradi-

ent at the gap edge of gas generates hydrodynamic instability such as Rayleigh instability (Chandrasekhar 1961; Papaloizou and Pringle 1984), Rossby wave instability (Li et al. 2001; Lin 2013), and baroclinic instability (Klahr & Bodenheimer 2003), which generate vortex and disturb the gas flow, which promote particle diffusion in radial direction, then particles can approach to the planet. The dynamics at the gap edge with particles has not been well understood, so detailed investigation on the gap dynamics is needed to understand solid accretion onto circumplanetary disks and resultant satellite formation.

Recently, Fujita et al. (2013) has investigated motion of planetesimals in heliocentric orbits in order to examine whether the planetesimals are captured by the circumplanetary disk of giant planets. They focus on planetesimals with size larger than that of ours, which means that gas drag is weak. They assume that the circumplanetary disk is axisymmetric around the planet and hydrostatic equilibrium in the direction perpendicular to the disk central plane, which is justified by their setting of large size objects. Although they do not obtain capture radius which we show in this paper, they consider non-zero initial eccentricity and inclination for the approaching objects. Fujita et al. (2013) and our work are thus in a mutually complementary relationship, and future works along the line of these studies will provide better understandings of satellite formation processes.

In this study, we observe that captured particles are rotating in prograde direction, and Johansen & Lacerda (2010) also showed that particles of a few cm in radius are rotating in prograde direction around protoplanets of a few hundred kilometers when the particles are captured by the protoplanets. Since particle density is much higher than gas density, particle motion seems to determine the rotating direction, whereas particles are dragged by gas that is rotating in prograde direction in our case. Although there is huge difference in mass for the two cases, we can observe common physical property that objects in a rotating frame tend to rotate in the same direction as the frame rotation by Coriolis force when they are pulled toward the center, as in tropical cyclones.

We have examined how particles in heliocentric orbits are captured by circumplanetary disks, but the captured particles, which are rotating in the similar velocity to that of the circumplanetary disk gas, are still migrating inward because of slight difference of the rotation velocities between gas and particles. This inward drift of particles in circumplanetary disks is important in the context of satellite formation because when the accretion rate of particles into the circumplanetary disks, which we have obtained, is given, the radial velocity determines the surface density of solid, which would then determine satellite growth rate. Assuming axisymmetric and isothermal for the circumplanetary disk, we can obtain rotation velocity of gas, gas drag force acting on the particles, and then inward migration velocity for the particles (Weidenschilling 1977; Nakagawa et al. 1986). For example, inward velocity for 1m particles is about 5ms^{-1} at 0.01 Hill radius from the planet, which corresponds to at $\sim 7R_J$ for a planet at 5AU. Applying the accretion rate given by Eq. (10) and assuming steady state inward particle flow,

we can estimate solid surface density as 1gcm^{-2} , which might be a bit small for satellite formation. However, the solid surface density estimated depends on particle size and gas density (which corresponds to f_H in this paper), and the drag law itself depends on the two parameters. Thus these dependences have to be examined in the future. In addition, size of particles in heliocentric orbits near giant planets is important for satellite formation processes because it affects accretion rate obtained in this study and the filtering effect for particles at the edge of gas gap produced by the giant planet. A recent statistical method that uses a coagulation equation with fragmentation showed that a large amount of particles of 1-100m in size are produced by fragmentation (Kobayashi et al. 2012). A comprehensive circumplanetary disk model that considers size distribution of incoming particles and growth in the disk would be necessary in the future in order to understand more realistic satellite formation processes.

Crida & Charnoz (2012) has recently proposed a totally different mechanism to reproduce the regular satellites. They considered a heavy and compact ring composed of small particles. Diffusion processes in the ring make it spread outward, and once particles are transported beyond the Roche limit, they are allowed to accumulate gravitationally to be a larger clump, which is a proto-satellite. The proto-satellite moves outward through tidal interaction with the planet and the ring, and once the proto-satellite migrates far enough, the second proto-satellite start to form. The ring produces many proto-satellites in this way. However, tidal interactions of outer (older) satellites are weaker, they migrate slower than inner ones, and tend to be captured by inner ones, which leads that outer satellites tend to be larger. Since this “pyramidal” size distribution is consistent with the current icy satellites around Saturn, Uranus, and Neptune, this mechanism would be likely to have occurred. This scenario need to have a heavy ring around the planet. Estrada & Mosqueira (2006) proposed a mechanism to supply solid materials into the Hill radius by collision between heliocentric planetesimals under gas-free condition, which may help to have a ring around the planet. In addition, this mechanism cannot explain Galilean satellites. Both mechanisms, formation from a gas disk with solid and formation from a ring without gas, have their advantages and disadvantages, so we may have to consider hybrid scenarios to explain the formation process of the current satellite systems.

5. CONCLUSIONS

We have demonstrated how solid particles in heliocentric orbits are captured by a circumplanetary disk around an actively growing giant planet embedded in a protoplanetary disk by using numerical integration of particle orbits with gas drag. We found that distance from the planet (orbital radius around the planet) when the particle is captured by the circumplanetary disk decreases with increasing particle size. The captured radius is approximated by a fitting function Eq. (6). The main contribution to the accretion is the regime where particles encounter with the planet in retrograde direction, which corresponds to the retrograde encounter regime in \tilde{b} space (Fig. 4). We also found that the accretion

efficiency is maximum when the size is $\sim 10^2$ m in the case of the surface density of the minimum mass solar nebula and 5AU planet. Width of the profile of normalized capture probability with respect to size is wide even in log scale (about two-order of magnitude in size). If the size is smaller than a critical size, particles cannot accrete onto the circumplanetary disk because of strong coupling with gas, which cannot accrete through the mid-plane even when active gas accretion phase. The size dependence of the accretion efficiency is approximated by Eq. (10). Even when a particle gap around the planet orbit is formed, captured radius is hardly affected by the gap, but accretion rate would be reduced and could be zero depending on the gap width. Several studies on the formation of particle gaps have been done. In particular, particle motion is strongly affected by the motion of gas, and the structure of the *gas* gap was not well understood at this stage mainly because the gas gap structure is affected by some hydrodynamic instability. Effect of the particle gap is important for satellite formation, and thus more studies on gas and particle gap should be done in the future.

We are grateful to Hidekazu Tanaka, Keiji Ohtsuki, Hiroshi Kobayashi, and Satoshi Okuzumi, Taku Takeuchi, Alessandro Morbidelli, Aurelian Crida for their valuable comments. We also thank the referee for comments that improve the manuscript. T.T. is supported by Grant-in-Aid for Scientific Research (23740326 and 24103503) from the MEXT of Japan. M.N.M. is supported by Grant-in-Aid for Scientific Research (25400232) from the MEXT of Japan. This work was supported by Center for Planetary Science running under the auspices of the MEXT Global COE Program entitled “Foundation of International Center for Planetary Science”. Numerical calculations were carried out on NEC SX-9 at Center for Computational Astrophysics, CfCA, of National Astronomical Observatory of Japan. A part of the figures were produced by GFD-DENNOU Library.

REFERENCES

- Adachi, I., Hayashi, C., & Nakazawa, K. 1976, *Prog. Theor. Phys.*, 56, 1756
- Ayliffe, B. A., & Bate, M. R. 2009, *MNRAS*, 397, 657
- Ayliffe, B. A., Laibe, G., Price, D. J., & Bate, M. R. 2012, *MNRAS*, 423, 1450
- Bate, M. R., Lubow, S. H., Ogilvie, G. I., & Miller, K. A. 2003, *MNRAS*, 341, 213
- Bodenheimer, P., & Pollack, J. B. 1986, *Icarus*, 67, 391
- Canup, R. M., & Ward, W. R. 2002, *AJ*, 124, 3404
- Canup, R. M., & Ward, W. R. 2006, *Nature*, 441, 834
- Chapman, S., & Cowling, T. G. 1970, Cambridge: University Press, 1970, 3rd ed.
- Chandrasekhar, S. 1961, *Hydrodynamic and Hydromagnetic Stability*, Clarendon press
- Crida, A., & Charnoz, S. 2012, *Science*, 228, 1196
- D’Angelo, G., Henning, T., & Kley, W. 2002, *A&A*, 385, 647
- D’Angelo, G., Kley, W., & Henning, T. 2003, *ApJ*, 586, 540
- Estrada, P., & Mosqueira, I. 2006, *Icarus*, 181, 486
- Estrada, P., Mosqueira, I., Lissauer, J. J., D’Angelo, G., & Cruikshank, D. P. 2009, in *Europa*, ed. R. T. Pappalardo, W. B. McKinnon, & K. Khurana (Tucson, AZ: Univ. Arizona Press), 27
- Fujita, T., Ohtsuki, K., Tanigawa, T., and Suetsugu, R. 2013, *AJ*, 146, 140
- Giuli, R. T. 1968, *Icarus*, 8, 301
- Gressel, O., Nelson, R. P., Turner, N. J., & Ziegler, U. 2013, *ApJ*, 779, 59
- Hayashi, C., Nakazawa, K., & Nakagawa, Y. 1985, *Protostars and planets II*, 1100
- Henon, M., & Petit, J.-M. 1986, *Celestial Mechanics*, 38, 67
- Ida, S., & Nakazawa, K. 1989, *A&A*, 224, 303
- Ida, S. 1990, *Icarus*, 88, 129
- Ikoma, M., Nakazawa, K., & Emori, H. 2000, *ApJ*, 537, 1013
- Inaba, S., Tanaka, H., Nakazawa, K., Wetherill, G. W., & Kokubo, E. 2001, *Icarus*, 149, 235
- Inaba, S., & Ikoma, M. 2003, *A&A*, 410, 711
- Iwasaki, K., & Ohtsuki, K. 2007, *MNRAS*, 377, 1763
- Johansen, A., & Lacerda, P. 2010, *MNRAS*, 404, 475
- Kley, W. 1999, *MNRAS*, 303, 696
- Kary, D. M., & Dones, L. 1996, *Icarus*, 121, 207
- Klahr, H., & Bodenheimer, P. 2003, *ApJ*, 582, 869
- Klahr, H., & Kley, W. 2006, *A&A*, 445, 747
- Kobayashi, H., Ormel, C. W., & Ida, S. 2012, *ApJ*, 756, 70 H., & Krivov, A. V. 2011, *ApJ*, 738, 35
- Korycansky, D. G., & Papaloizou, J. C. B. 1996, *ApJS*, 105, 181
- Li, H., Colgate, S. A., Wendroff, B., & Liska, R. 2001, 551, 874
- Lin, M. 2013, *ApJ*, 765, 84
- Lubow, S. H., Seibert, M., & Artymowicz, P. 1999, *ApJ*, 526, 1001
- Lunine, J. I., & Stevenson, D. J. 1982, *Icarus*, 52, 14
- Machida, M. N., Matsumoto, T., Tomisaka, K., & Hanawa, T. 2005, *MNRAS*, 362, 369
- Machida, M. N., Kokubo, E., Inutsuka, S., & Matsumoto, T. 2008, *ApJ*, 685, 1220
- Machida, M. N., Kokubo, E., Inutsuka, S., & Matsumoto, T. 2010, *MNRAS*, 405, 1227
- Matsumoto, T., & Hanawa, T. 2003, *ApJ*, 595, 913
- Miki, S. 1982, *Prog. Theor. Phys.*, 67, 1053
- Mizuno, H. 1980, *Prog. Theor. Phys.*, 64, 544
- Morbidelli, A., & Nesvorný, D. 2012, *A&A*, 546, 18
- Mosqueira, I., & Estrada, P. R. 2003, *Icarus*, 163, 198
- Muto, T., & Inutsuka, S. 2009, *ApJ*, 695, 1132
- Nakagawa, Y., Sekiya, M., & Hayashi, C. 1986, *Icarus*, 67, 375
- Nakazawa, K., & Ida, S. 1988, *Prog. Theor. Phys. Suppl.*, 96, 167
- Nishida, S. 1983, *Prog. Theor. Phys.*, 70, 93
- Ohtsuki, K. 1999, *Icarus*, 137, 152
- Ohtsuki, K., Stewart, G. R., & Ida, S. 2002, *Icarus*, 155, 436
- Okuzumi, S., Tanaka, H., Kobayashi, H., & Wada, K. 2012, *ApJ*, 752, 108
- Paardekooper, S.-J. 2007, *A&A*, 462, 355
- Paardekooper, S.-J., & Mellema, G. 2008, *A&A*, 478, 245
- Papaloizou, J. C. B., & Pringle, J. E. 1984, *MNRAS*, 208, 721
- Petit, J. M., & Henon, M. 1986, *Icarus*, 66, 536
- Press, W. H., Teukolsky, S. A., Vetterling, W. T., & Flannery, B. P. 2007, *Numerical Recipes 3rd Edition: The Art of Scientific Computing*
- Rice, W. K. M., Armitage, P. J., Wood, K., and Lodato, G. 2006, *MNRAS*, 373, 1619
- Sekiya, M., Miyama, S., & Hayashi, C. 1987, *EM&P*, 39, 1
- Shakura, N. I., & Sunyaev, R. A. 1973, *A&A*, 24, 337
- Shiraishi, M., & Ida, S. 2008, *ApJ*, 684, 1416
- Szulagyi, J., Morbidelli, A., Crida, A., & Masset, E. 2014, accepted for publication in *ApJ*
- Tanaka, H., & Ida, S. 1997, *Icarus*, 125, 302
- Tanigawa, T., & Watanabe, S. 2002, *ApJ*, 580, 506
- Tanigawa, T., & Ohtsuki, K. 2010, *Icarus*, 205, 658
- Tanigawa, T., Ohtsuki, K., & Machida, M. N. 2012, *ApJ*, 747, 47
- Watanabe, S., & Ida, S. 1997, Sec. 3 of *Comparative Study of Planetology*, Vol. 12 of Earth and Planetary Science series (in Japanese), Iwanami Shoten Publishers
- Ward, W. R. 2009, in *Lunar and Planetary Institute Science Conference Abstracts*, the Woodlands, Texas: Lunar and Planetary Science, 40, 1477
- Ward, W. R., & Canup, R. M. 2010, *AJ*, 140, 1168
- Weidenschilling, S. J. 1977, *MNRAS*, 180, 57
- Youdin, A. N., & Lithwick, Y. 2007, *Icarus*, 192, 588
- Zhou, J., & Lin, D. N. C. 2007, *ApJ*, 666, 447
- Zhu, Z., Nelson, R. P., Dong, R., Espaillat, C., & Hartman, L. 2012, *ApJ*, 755, 6